Realizing Optical Magnetism from Dielectric Metamaterials

James C. Ginn* and Igal Brener
Sandia National Laboratory, Albuquerque, New Mexico 87185, USA, and Center for Integrated Nanotechnologies, Sandia National Laboratory, Albuquerque, New Mexico 87185, USA

David W. Peters, Joel R. Wendt, Jeffrey O. Stevens, Paul F. Hines, Lorena I. Basilio, Larry K. Warne, Jon F. Ihlefeld, Paul G. Clem, and Michael B. Sinclair
Sandia National Laboratory, Albuquerque, New Mexico 87185, USA
(Received 7 October 2011; published 29 February 2012)

We demonstrate, for the first time, an all-dielectric metamaterial composite in the midinfrared based on micron-sized, high-index tellurium dielectric resonators. Dielectric resonators are desirable compared to conventional metallodielectric metamaterials at optical frequencies as they are largely angular invariant, free of Ohmic loss, and easily integrated into three-dimensional volumes. Measurements and simulation provide evidence of optical magnetism, which could be used for infrared magnetic mirrors, hard or soft surfaces, and subwavelength cavities.

DOI: 10.1103/PhysRevLett.108.097402 PACS numbers: 78.67.Pt, 81.07.−b, 85.50.−n

The unique properties of metamaterials have yielded many exciting optical phenomena including sub-diffraction-limited imaging [1], cloaking [2], and perfect absorption [3]. As part of this development, considerable interest has been focused on the development of metamaterials that exhibit artificial optical magnetism for applications in negative-refraction materials [4], magnetic mirrors [5], hard or soft surfaces [6], and subwavelength cavities [7]. Despite rapid advances in this field, passive metamaterials at optical frequencies have often proven impractical due to significant conductor loss from the metallic resonators comprising these volumes [8]. Moreover, the inherent geometrical asymmetry of these resonators further restricts metamaterial behavior to a small range of incident angles even when they are assembled into three-dimensional structures [9]. Three-dimensional dielectric resonators, unlike their metallic counterparts, have significantly less material loss, support resonant modes that are invariant to the excitation angle, and can be easily integrated into thick volumes [10]. In this Letter, we describe the development of a dielectric-resonator-based metamaterial in the midwave infrared with negative magnetic effective properties. Additional insight is also provided in addressing material limitations imposed on dielectric metamaterials at optical frequencies.

Lewin [11] was one of the first to theoretically demonstrate that a periodic array of nonmagnetic, subwavelength dielectric spheres in a nonmagnetic medium can exhibit spectral regions of Lorentzian-like effective permeability in accordance with Mie theory [12]. It can be shown from Lewin's work that magnetic activity (negative permeability) can be achieved in this array when [13]

$$-\frac{2+f}{1-f} < \frac{2(\sin\theta - \theta\cos\theta)}{(\theta^2-1)\sin\theta + \theta\cos\theta} < -2\frac{1-f}{1+2f}, \quad (1)$$

where θ is equal to $k_0 a\sqrt{\epsilon_i}$, the packing fraction f is defined as $4\pi a^3/3s^3$, and a is the radius of the sphere, s is the sphere's period, k_0 is the vacuum wave number, and ϵ_i is the permittivity of the inclusion. Thus, the effective magnetic polarizability of these arrays can be engineered by altering the dimensions, composition, and packing fraction of the spherical inclusions.

Utilizing spherical inclusions for magnetic media at optical frequencies is undesirable from the standpoint of lithography; however, similar behavior has been shown using high-index cubic dielectric resonators (CDRs) [14]. In Fig. 1, the analytically determined on-resonance field distribution of an isolated sphere is compared to that of a cubic resonator array (Fig. 1(a)) calculated using the

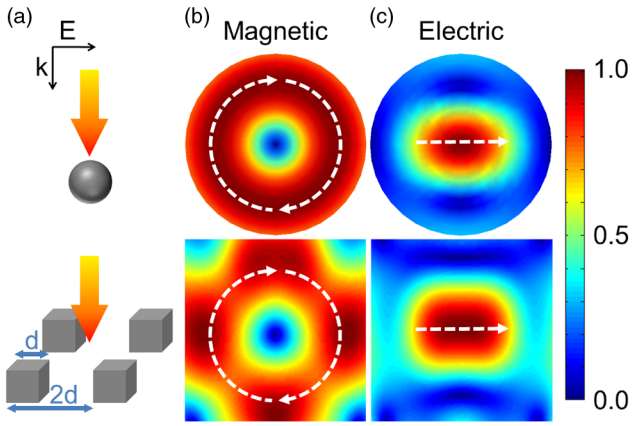

FIG. 1 (color online). (a) Excitation configuration of an isolated sphere (top row) and an infinite two-dimensional cube array with 1:1 duty cycle (bottom row). Normalized electric field distribution is shown for the (b) first- and (c) second-order modes in the sphere and cubic resonators. White dashed lines and arrows indicate field direction.

commercially available rigorous coupled wave analysis package, GD-CALC (using 961 Floquet modes for convergence). Like the spherical resonator, the lowest-order mode of a CDR is a magnetic dipole (TE_{011}). The electric field profile shown in Fig. 1(b) for the cube array is nearly identical to the mode profile observed in finite-difference-time-domain simulations of scattering from isolated cubes and indicates that interactions with neighboring cubes induce only minor perturbations of the mode shape. Analysis of the far-field scattering profile for similar cubes reveals that this mode corresponds to a magnetic dipole [15]. This is not surprising since there is a displacement current loop associated with the circulating electric field seen in Fig. 1(b) that is the analog of the conduction current loop in split ring resonators. The second-lowest mode is an electric dipole (TM_{011}) [14] for which the linear electric field distribution shown in Fig. 1(c) (and corresponding displacement current) leads to electric dipole far-field behavior. The electromagnetic response of cubic resonators is isotropic in the quasistatic regime and is slightly less isotropic when phase advance of the incident wave across the cube dimension is included. Nevertheless, the response of cubic resonators is much more isotropic than that of metallic resonators, and the tensor form of the effective permeability of a CDR array is dominated by the lattice arrangement of the elements. Also, whereas significant damping due to Ohmic loss is unavoidable for metallic resonators in the infrared, the damping of dielectric resonators can be quite low provided the resonator material lacks free carriers or phonon modes in the band of interest.

Identification of candidate low-loss resonator materials is critical in designing a practical infrared CDR metamaterial. In addition, the CDR material must possess a large index of refraction to ensure that the dimensions of the resonator and array spacing are sufficiently subwavelength to avoid diffraction. Only two classes of dielectrics exhibit positive indices of refraction greater than 3 in the optical portion of the spectrum: highly crystalline polaritonic materials and narrow band-gap (< 1.5 eV) materials. Metamaterial structures using polaritonic materials have previously been investigated [16], but these materials are less desirable due to their high loss at the phonon resonance and limited spectral flexibility. In contrast, narrow band-gap materials exhibit large indices over wide spectral bands and experience significant loss near the band-gap only at shorter wavelengths and on the tail of the free-carrier absorption at longer wavelengths. Candidate narrow band-gap materials for infrared CDR designs include silicon [17], germanium, tellurium, and IV-VI compounds containing lead (such as lead telluride).

Initial investigations of a magnetic active CDR array in the infrared were carried out using germanium cubes on a low-index polymer thin film [18]. Tellurium (Te) was subsequently selected as a better resonator material due to its larger index of refraction and low loss at infrared wavelengths [19]. Because of its trigonal crystal lattice [20], a polycrystalline morphology is preferable which yields a crystal-averaged index of refraction of 5.3 at 10 μm, with an extinction coefficient of less than 10^{-4} [21]. Barium fluoride (BaF_2) was selected as the optimal substrate due to its low refractive index (~ 1.4) and low loss at 10 μm.

Through simulation, a 1.7 μm CDR with a 3.4 μm unit-cell spacing (1:1 duty cycle) was chosen to center the reflection peak of the magnetic resonance at 10 μm. A 1.7 μm thick film of Te was deposited on the surface of a BaF_2 optical flat via electron-beam evaporation, patterned using electron-beam lithography, and etched using a reactive ion etching process. A scanning electron micrograph of the etched pattern is shown in Fig. 2(a). The final CDR element was 1.7 μm tall with a 1.53×1.53 μm base and a 10° sidewall slope. Ellipsometric analysis yielded a fitted complex index of refraction of $n = 5.02 + i0.04$ for the Te films at 10 μm.

Following fabrication, the patterned wafer was characterized using a hemispherical directional reflectometer). The measured collimated transmission and specular reflection of the array are plotted in Fig. 2(b). As expected from the fabricated topology, the reflection peak of the magnetic resonance was slightly down-shifted to 9 μm. The optical

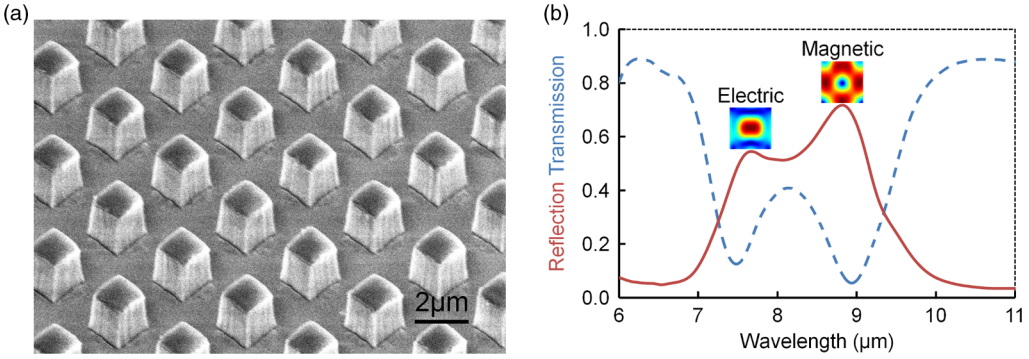

FIG. 2 (color online). (a) Scanning electron micrograph of a fabricated CDR array. (b) Measured reflection (solid [red] curve) and transmission (dashed [blue] curve) coefficients for the CDR array. Field patterns from Fig. 1 are shown above each corresponding resonance.

response of the fabricated CDR array was simulated using a cube dimension of 1.45 μm, which was chosen to yield the same volume as the as-made resonators (Fig. 3(a)). Both the simulation and the experiment clearly show two resonances with corresponding peaks in the reflection coefficient and minima in the transmission coefficient. The magnetic resonance in the simulated coefficients is at 8.9 μm and shows good agreement with the experimentally observed feature at 9 μm. However, simulations predict an electric resonance at 6.75 μm which is experimentally observed near 7.5 μm. Subsequent simulations using rectangular resonators and resonators with tapered walls did not remove this discrepancy, which possibly arises from the nonuniformity of the as-fabricated cube and the presence of a capping layer that formed during etching.

Figure 3(b) shows the impedance phase of the CDR, calculated using

$$\Phi = -i \ln\left(\frac{1}{A}\sqrt{\frac{(1+r)^2 - t^2}{(1-r)^2 - n_s^2 t^2}}\right), \tag{2}$$

where A is a real valued amplitude, r and t are the simulated Fresnel reflection and transmission coefficients, and n_s is

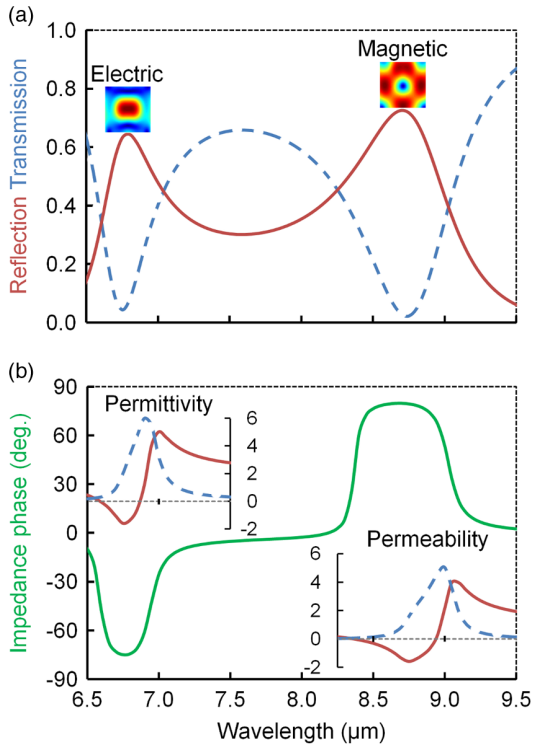

FIG. 3 (color online). (a) Plot of simulated reflection (solid [red] curve) and transmission (dashed [blue] curve) for the CDR array. (b) Plot of the calculated impedance phase (central [green] curve), permittivity, and permeability for the simulated CDR array. Real values are solid (red) lines and imaginary values are dashed (blue) lines.

the frequency-dependent index of refraction of BaF_2. Positive impedance phase occurs when the permeability is less than zero, and negative impedance phase occurs when the permittivity is less than zero. The CDR array can be treated as a nonideal conductor when the wave impedance becomes predominately imaginary (i.e., the impedance phase approaches ± 90 degrees). From boundary conditions, when the impedance is imaginary and the impedance phase is positive, the array will behave as a magnetic conductor and the magnetic field of an incident wave will experience a 180° phase shift upon reflection. Conversely, when the impedance is imaginary and the impedance phase is negative, the array will behave as an electric conductor and the electric field will experience a 180° phase shift upon reflection. This behavior was independently confirmed by simulating the reflected phase front from the fabricated CDR array at the two resonances and verifying that the reflected electric field is in-phase with the incident field at the magnetic resonance, and 180° out-of-phase with the incident field at the electric resonance.

To further validate the distinct magnetic and electric behavior, a standard algorithm [22] was used to retrieve the effective permittivity and permeability in the vicinity of the two resonances [insets to Fig. 3(b)]. Both the effective permeability and the effective permittivity reach values of less than -1 in spectral regions where the array can be described as an effective medium (to be discussed below). The loss tangent of the permeability falls to 0.48 when the real part of permeability is equal to -1. We anticipate that significantly lower-loss metamaterials will be achievable as we continue to improve the quality of our Te films by removing the capping layer formed during etching, improving film uniformity (ellipsometry indicated a degree of grading), and reducing absorption. (The measured absorption loss for our films is 2 orders larger than the literature value [21].)

To further investigate the features of optical CDRs, a series of rigorous coupled wave analysis simulations was run for a 1:1 duty-cycle array while varying only the refractive index of the cubes. The solid diagonal lines in Fig. 4 denote the normalized wavelength at the points of peak reflectivity due to the two primary resonances, versus index of refraction (restricted to a range of values that is realistic for optical materials). As the frequency of the incident wave approaches the magnetic resonance from the low-frequency side (i.e., moving downward in Fig. 4), the effective permeability increases, leading to an increase in the effective refractive index and a corresponding decrease in the effective wavelength. In the immediate vicinity of the resonance, the phase advance of the wave across the unit cell becomes significant and spatial dispersion effects appear [23–26]. When the effective wavelength in the CDR array becomes equal to the array period (i.e., when $n_{\text{eff}} = \lambda/d$), a photonic crystal bandgap regime is encountered [23–26] for which field homogenization breaks down and retrieved optical

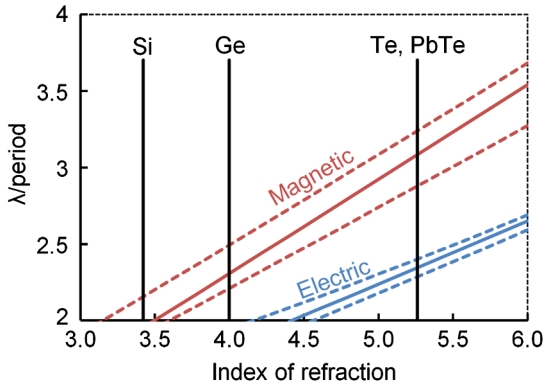

FIG. 4 (color online). Design metric for 1:1 CDR metamaterials. Solid lines correspond to the lowest-order magnetic and electric resonances, as labeled above each set of lines. The top dashed line for each resonance defines the transition to a band-gap regime, and the bottom dashed line defines where the effective parameter has its zero crossing. The indices of several materials at 10 μm are also labeled.

properties no longer hold physical meaning [25,26]. From our simulations, we have observed that the low-frequency boundary of this regime coincides with the peak of the effective permeability that we obtained using the standard retrieval algorithm [22]. This boundary is denoted by the dashed line above the magnetic resonance line in Fig. 4. Between this boundary and the resonance line, the retrieval algorithm yields unphysical (acausal, nonpassive) results for the permittivity [23–26]. Beyond the resonance line, the behavior of the array becomes dominated by a plasma mode (i.e., $\mathrm{Re}(\mu_{\mathrm{eff}}) < 0$) and spatial dispersion effects begin to decrease. The plasma regime persists until the zero crossing of the real part of the effective permeability (denoted by the dashed line below the magnetic resonance line in Fig. 4) where the array once again supports a propagating mode. A corresponding set of boundary lines is shown in Fig. 4 for the electric resonance.

The significance of these band-gap and spatial dispersion effects increases as the permittivity of the resonator decreases since the size of the resonator and unit cell must grow relative to the operating wavelength. The limitations imposed by these effects are more severe in the optical and infrared regimes as compared to the rf and THz portions of the spectrum, since the maximum identified permittivities available in the infrared are $\sim$35, while materials with substantially larger permittivities are available in the rf and THz [14]. Band-gap and spatial dispersion effects severely limit the practicality of silicon- and germanium-based dielectric metamaterials in the midwave infrared.

In this Letter, we have described the design, fabrication, and characterization of a dielectric cubic resonator metamaterial with magnetic activity in the midinfrared. Through theory and simulation, a generalized design approach for metamaterial surfaces comprising cubic resonators at optical frequencies has been developed. This work represents a first step toward the development of passive low-loss, isotropic artificial magnetic conductors, magnetic mirrors, hard or soft surfaces, and subwavelength cavities in the infrared.

This research was supported by the Laboratory Directed Research and Development program at Sandia National Laboratories. This work was performed, in part, at the Center for Integrated Nanotechnologies, a U.S. Department of Energy, Office of Basic Energy Sciences user facility. Sandia is a multiprogram laboratory operated by Sandia Corporation, a Lockheed Martin Company, for the U.S. Department of Energy under contract DE-AC04-94AL85000.

*Present address: Plasmonics, Inc., Orlando, FL 32826, USA
james.ginn@plasmonics-inc.com

[1] J. B. Pendry, Phys. Rev. Lett. **85**, 3966 (2000).
[2] D. Schurig, J. J. Mock, B. J. Justice, S. A. Cummer, J. B. Pendry, A. F. Starr, and D. R. Smith, Science **314**, 977 (2006).
[3] N. I. Landy, S. Sajuyigbe, J. J. Mock, D. R. Smith, and W. J. Padilla, Phys. Rev. Lett. **100**, 207402 (2008).
[4] V. G. Veselago, Phys. Usp. **10**, 509 (1968).
[5] A. S. Schwanecke, V. A. Fedotov, V. V. Khardikov, S. L. Prosvirnin, Y. Chen, and N. I. Zheludev, J. Opt. A **9**, L1 (2007).
[6] P.-S. Kildal, Electron. Lett. **24**, 168 (1988).
[7] N. Engheta, IEEE Antennas Wireless Propag. Lett. **1**, 10 (2002).
[8] S. Xiao, V. P. Drachev, A. V. Kildishev, X. Ni, U. K. Chettiar, V. M. Yuan, and H.-K. Shalaev, Nature (London) **466**, 735 (2010).
[9] D. B. Burckel, J. R. Wendt, G. A. Ten Eyck, J. C. Ginn, A. R. Ellis, I. Brener, and M. B. Sinclair, Adv. Mater. **22**, 5053 (2010).
[10] R. D. Rasberry, Y.-J. Lee, J. C. Ginn, P. F. Hines, C. L. Arrington, A. E. Sanchez, M. T. Brumbach, P. G. Clem, D. W. Peters, M. B. Sinclair, and S. M. Dirk, J. Mater. Chem. **21**, 13902 (2011).
[11] L. Lewin, J. Inst. Electr. Eng. **94**, 65 (1947) [http://ieeexplore.ieee.org/xpl/freeabs_all.jsp?arnumber=5298931].
[12] C. F. Bohren and D. R. Huffman, *Absorption and Scattering of Light by Small Particles* (John Wiley & Sons, New York, 1983).
[13] C. Holloway, E. Kuester, J. Baker-Jarvis, and P. Kabos, IEEE Trans. Antennas Propag. **51**, 2596 (2003).
[14] Q. Zhao, L. Kang, B. Du, H. Zhao, Q. Xie, X. Huang, B. Li, J. Zhou, and L. Li, Phys. Rev. Lett. **101**, 027402 (2008).
[15] L. A. Warne, L. I. Basilio, W. L. Langston, W. A. Johnson, and M. B. Sinclair, IEEE Trans. Antennas Propag. (to be published).
[16] J. A. Schuller, R. Zia, T. Taubner, and M. L. Brongersma, Phys. Rev. Lett. **99**, 107401 (2007).

[17] K. Vynck, D. Felbacq, E. Centeno, A. I. Cabuz, D. Cassagne, and B. Guizal, Phys. Rev. Lett. **102**, 133901 (2009).

[18] J. C. Ginn, G. A. Ten Eyck, I. Brener, D. W. Peters, and M. B. Sinclair, in *Photonic Metamaterials and Plasmonics*, OSA Technical Digest (CD), paper MWD2 (Optical Society of America, Washington, DC, 2010) [http://www.opticsinfobase.org/abstract.cfm?uri=PMETA_PLAS-2010-MWD2].

[19] Y. Fink, J. N. Winn, S. Fan, C. Chen, J. Michel, J. D. Joannopoulos, and E. L. Thomas, Science **282**, 1679 (1998).

[20] E. Weidmann and J. Anderson, Thin Solid Films **7**, 265 (1971).

[21] E. D. Palik, *Handbook of Optical Constants of Solids II* (Academic Press, San Diego, CA, 1998), p. 709.

[22] D. R. Smith, S. Schultz, P. Markos, and C. M. Soukoulis, Phys. Rev. B **65**, 195104 (2002).

[23] R. Liu, T. J. Cui, D. Huang, B. Zhao, and D. R. Smith, Phys. Rev. E **76**, 026606 (2007).

[24] A. Alù, Phys. Rev. B **84**, 075153 (2011).

[25] C. R. Simovski, J. Opt. **13**, 013001 (2011).

[26] C. R. Simovski, Opt. Spectrosc. (USSR) **107**, 726 (2009).